Available online at www.sciencedirect.com
SCIENCE DIRECT®
Computers and Structures 83 (2005) 2238–2256
Computers & Structures
www.elsevier.com/locate/compstruc

A plastic damage approach for confined concrete

B.M. Luccioni [a,b,*], V.C. Rougier [b]

[a] CONICET, Av. Rivadavia 1917, Buenos Aires, Argentina
[b] Structures Institute, National University of Tucumán, Av. Roca 1800, S.M. de Tucumán, Argentina

Received 11 February 2004; accepted 23 March 2005
Available online 28 June 2005

Abstract

There are many situations in which it is necessary to increase the capacity of structures in use. This need maybe either for a change of use or because the structures have suffered some damage or have shown little resistance in case of extreme loads such as earthquakes. The most common methods for repair and retrofit of reinforced concrete columns are concrete jacketing, steel jacketing and fiber wrapping. This last type of reinforcement has many advantages as it offers a high-strength, low-weight and corrosion-resistant jacket with easy and rapid installation. The reinforcement with composite materials improves shear and compression strength and ductility as a result of concrete core confinement. The present analytical and numerical ability to quantify the efficiency of fiber confinement is rather limited, especially with respect to ductility.

A constitutive model that approximately reproduces the behavior of structural concrete elements under confinement is developed in this paper. The model allows the assessment of concrete columns and bridge piles repaired and/or reinforced with fiber reinforced composites (FRP). The model presented is a modification of an existing coupled plastic damage model. A new definition for the plastic hardening variable and a new yielding surface with curved meridians are proposed. Both improvements enable the adequate reproduction of concrete behavior in high confinement conditions.

The comparison of numerical and experimental results shows the model capacity to simulate concrete behavior under triaxial compression conditions like the ones present in concrete columns confined with fiber reinforced composites.

Keywords: Concrete; Confinement; Fiber reinforced composites; Plasticity; Damage; Dilation

1. Introduction

There are a number of situations where it may become necessary to increase the load-carrying capacity of a structure in service. These situations include change of loading or usage, and the cases of structures that have been damaged. Deterioration of reinforced concrete (RC) columns due to corrosion of the reinforcing steel and spalling of concrete has been a major problem for the aging infrastructure [1].

The most common methods for repair and retrofit of RC columns are concrete jacketing, steel jacketing and fiber wrapping. FRP reinforcement has many advantages, as it offers a high-strength, low-weight and

* Corresponding author. Tel./fax: +54 381 4364087.
E-mail address: bluccioni@herrera.unt.edu.ar (B.M. Luccioni).

0045-7949/$ - see front matter © 2005 Elsevier Ltd. All rights reserved.
doi:10.1016/j.compstruc.2005.03.014

corrosion-resistant jacket with easy and rapid installation and minimal change in the column geometry. In particular, carbon FRP, of all the composites, shows high durability and an E-modulus comparable to steel or even higher. Also, fiber wrapping does not require access for heavy vehicles such as cranes, contrary to the other two methods [2].

The wrap enhances shear strength, axial strength and ductility of the column. It produces lateral strain restrictions that react to the Poisson-type lateral expansion tendencies of the concrete core, and generates side pressures, i.e. confinement. For flexural strengthening, fiber reinforced polymer (FRP) sheets or near-surface-mounted FRP rods can be bonded to the column in the axial direction [2].

During the past decade efforts have been increasingly concentrated on the replacement of the conventional steel reinforcement in concrete elements by fiber reinforced polymer (FRP) reinforcement. Since the first application of fiber wrapping on concrete chimneys in Japan [2], there has been a number of studies on the use of this technique. The method has been put into practice with great success in several states such as California, Nevada and New York. Both carbon and glass fibers have been used in a variety of forms such as fabric, straps, cable and pre-cured forms.

The structural effectiveness of FRPs in the rehabilitation of existing structural systems has repeatedly been demonstrated with full or large-scale structural tests at the University of California, San Diego (UCSD) [3]. Carbon fabric overlays have been used to strengthen and retrofit reinforced and unreinforced masonry walls for seismic loads, as well as to restore and more than double the displacement capacity in the repair of a full-scale five-story reinforced masonry building tested to failure under simulated seismic loads. Carbon fiber overlays and strips have also been used to strengthen reinforced concrete slabs (with and without openings) and to strengthen large diameter prestressed concrete pipelines to restore loss of load (water pressure)-carrying capacity due to corrosion of the prestressing wires. Bridge columns have been seismically retrofitted and repaired with fiberglass, carbon and hybrid composite jackets, which were shown to be as effective as conventional steel jackets.

The experimental investigation of the performance of FRP sheet confinement shows that it can effectively enhance the strength and ductility of concrete as well as energy absorption, even at low volumetric ratios [4]. FRP reinforcement exhibits an almost linear elastic behavior up to failure that ensures an ever-increasing confining pressure on the concrete core. The stiffness of the confinement constitutes one of the most important design parameters. Recently, Shao and Mirmiran [5] evaluated the implications of using FRP as primary and sole reinforcement for concrete structures in seismic regions through an experimental and analytical investigation on the cyclic response of two different types of laminated glass FRP tubes filled with concrete. The study showed that concrete-filled tubes can be designed with an appropriate laminate structure for a ductility level comparable to that of conventional reinforced concrete columns.

The present analytical ability to quantify the behavior of FRP confined concrete columns is rather limited, especially with respect to ductility. As a result, code requirements on reinforcement may be too conservative in most cases, and may still be insufficient for some situations of extensive deformations caused by severe earthquake loads [6].

Concrete under stress is probably among the least understood (until a few years ago) and most extensively modelled structural materials. At present the mechanical behavior of concrete demonstrates a wide range of unusual features that cannot be completely described by classical constitutive theories of elasticity and plasticity and make concrete a difficult material to model.

The objective of this paper is to present a constitutive model for concrete under triaxial stresses that predicts the load-deformation material response under different load combinations fairly accurately. The use of this model in a nonlinear finite element program in combination with an orthotropic elastic brittle model for FRP sheets allows for more reliable quantitative calculations of the strength and ductility of FRP confined concrete columns.

The model is based on a coupled plastic damage theory [7] that can accurately reproduce the behavior of confined concrete. The model takes into account the specific characteristics of the dilatational response of confined concrete. The predictions of the model are compared against the experimental data of different strength concretes under triaxial compression and FRP confined concrete columns. From the comparison it can be concluded that the predicted behavior of concrete and that of the composite system is accurate enough for a wide range of materials strength and amount of confinement.

2. Behavior of concrete confined with fiber composites

2.1. Behavior of concrete under triaxial compression

Concrete is a non-homogeneous, anisotropic material whose response is nonlinear even under small stress levels. Furthermore, concrete exhibits a different behavior under tension and compression stresses. In compression, the response hardens up to a peak stress value that depends on the level of lateral confinement. The post-peak behavior depends in general on the level of lateral confinement. Under low confinement, the post-peak response is brittle softening. For increasing confinement

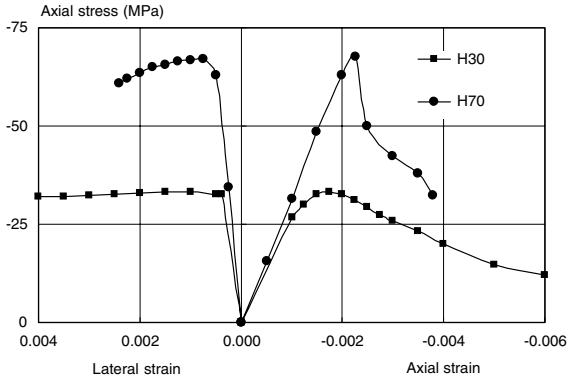

Fig. 1. Stress–strain curves for different strength concretes (H30 and H70) under uniaxial compression [9].

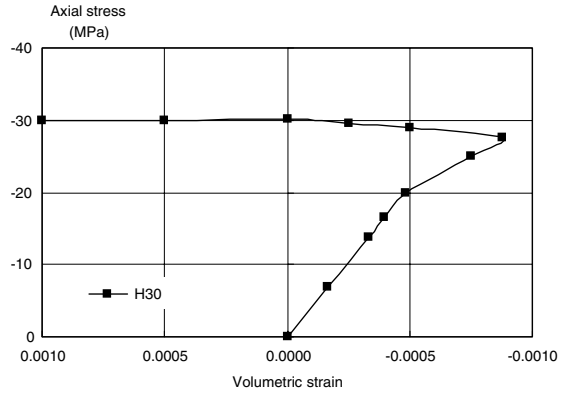

Fig. 2. Stress vs volumetric strain curve for a normal strength concrete under uniaxial compression [12].

stresses, the response of concrete changes to ductile hardening. Under tensile stresses, concrete cracks and eventually loses strength entirely [8].

Fig. 1 shows the stress–strain curves for two different strength concretes [9]. The initial slope of the stress–strain curve that represents the stiffness in the undamaged concrete under uniaxial compression increases with an increase in the nominal compressive strength. It seems that these differences in the initial stiffness can be linked directly to the differences in internal structure, the most descriptive and prominent measure of which is the degree of porosity. This suggests the concept of an upper-bound strength, associated with a virtual zero-void condition [10,11].

As imposed axial strain increases, damage starts to accumulate in the material structure, manifested by a deviation from the linear elastic response in the strain–stress plot. Although no linearity is delayed in all aspects of the behavior of higher-strength concretes, once it starts, it occurs at a much faster rate than for lower strength material. The post-peak response is, therefore, characterized by a sudden decay [10,11].

Fig. 2 shows the curve relating volumetric strains with axial stress for a normal strength concrete [12]. The idealized elastic behavior would predict a net contraction. However, the post-peak range of the stress–strain response is characterized by the complete reversal of volumetric strains into the range of volumetric expansion (dilation). This point, which marks the onset of a dramatic loss of resistance, is a critical milestone in the behavior of concrete because it also identifies the onset of uncontrolled crack propagation and growth that under normal testing of high-strength materials is almost instantaneous [10,11].

Confinement is known to delay loss of stiffness and strength and to increase the deformability of concrete. The results of concrete compression tests under different confinement pressures [12] are shown in Fig. 3. The

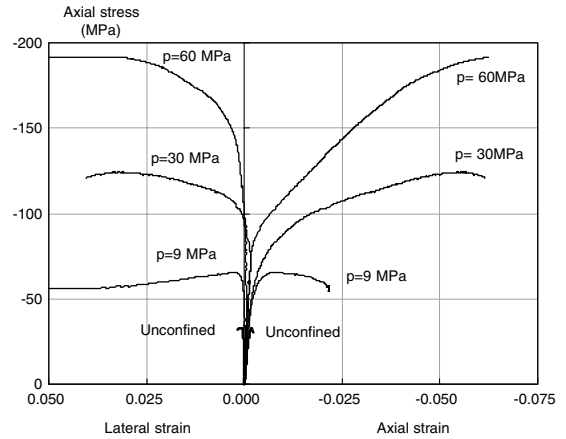

Fig. 3. Stress–strain curves obtained from compression tests on a normal strength concrete under different confinement pressures [12].

higher internal stress and higher deformability developed by the confined concrete simply imply a delay in the onset of unstable crack propagation. Evidently, confinement provides the necessary lateral kinematic restraint that prevents volumetric dilation and keeps the concrete fragments together, to an extent that failure can be delayed. Fig. 4 shows the volumetric response of concrete under different confinement pressures [12]. It can be observed that dilatation can be totally prevented in compression tests under very high confining pressures.

The response of concrete under triaxial compression greatly depends on the formation and expansion of microcracks. Several test programs have shown that the evolution of the microcracks governs the concrete brittleness, ductility, dilatancy and failure modes. All these phenomena depend in general on the triaxial state of stress applied to the concrete. Under low lateral

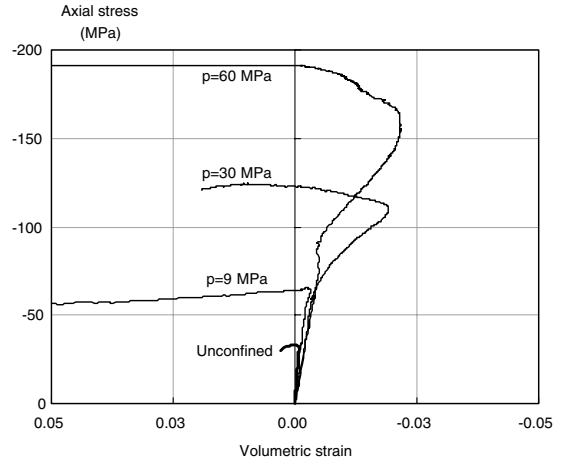

Fig. 4. Stress vs volumetric strain curve obtained from compression tests on a normal strength concrete under different confinement pressures [12].

confinement, failure in compression tests is caused by vertical tension splitting. A sharp post-peak loss of strength is observed. Under gradually larger confinement, cracking and damage become more distributed and concrete becomes ductile, with little or no post-peak degradation [8].

2.2. FRP confinement

Fig. 5 shows the response curves of cylindrical concrete specimens confined by glass fiber reinforced composites [13,14] and indicates a significant enhancement in strength and ductility of concrete. Furthermore, unlike steel-encased concrete, response of FRP-encased concrete is almost bilinear with no descending branch

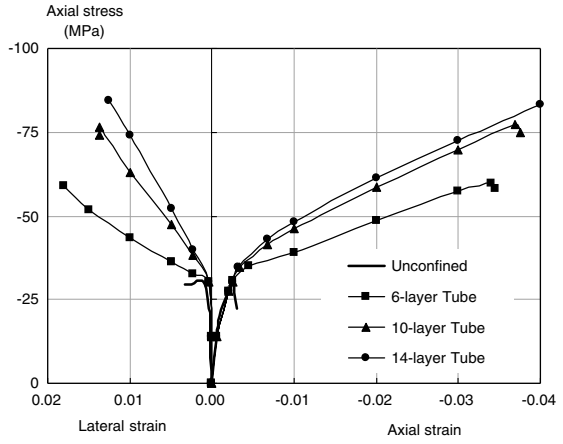

Fig. 5. Stress–strain curves for concrete confined with GFRP tubes [13,14].

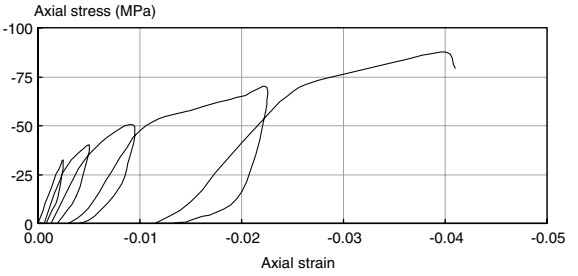

Fig. 6. Uniaxial cyclic compression response of GFRP-encased concrete [13,14].

[13]. This difference is due to the elastic behavior of FRP composites. The response consists of three distinct regions. In the first region, the behavior is similar to that of plain concrete, since lateral expansion of the core is insignificant. With the increase in microcracks, a transition zone is entered where the tube exerts a lateral pressure on the core to counteract the stiffness degradation of concrete. Finally, a third region is recognized in which the tube is fully activated, and the stiffness is generally stabilized around a constant rate. The response in this region is mainly dependent on the stiffness of the tube.

Fig. 6 shows the results obtained for FRP-encased concrete under quasistatic cyclic load [13,14]. The stress–strain path obtained for monotonically increasing load may serve as an envelope for the case of cyclic load characterized by loading and unloading branches forming loops. While the loops become wider beyond the peak strength of unconfined concrete, stiffness degradation is not as severe as that of steel-encased concrete.

The volumetric response of FRP-encased concrete [13,14] is shown in Fig. 7. Despite some volume expansion beyond the critical stress of confined concrete, the linearly increasing hoop stress of FRP eventually curtails the volume expansion and reverses its direction. It

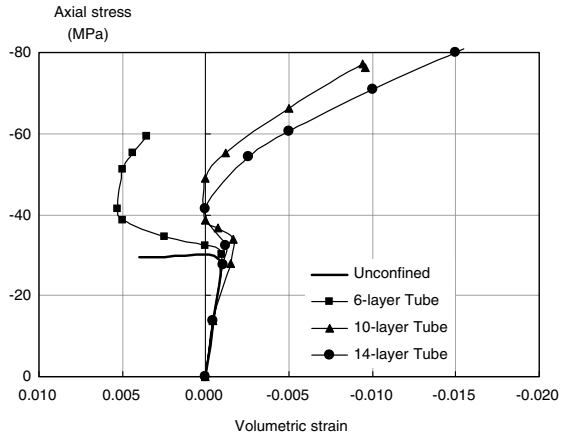

Fig. 7. Volumetric strains of GFRP-encased concrete [13,14].

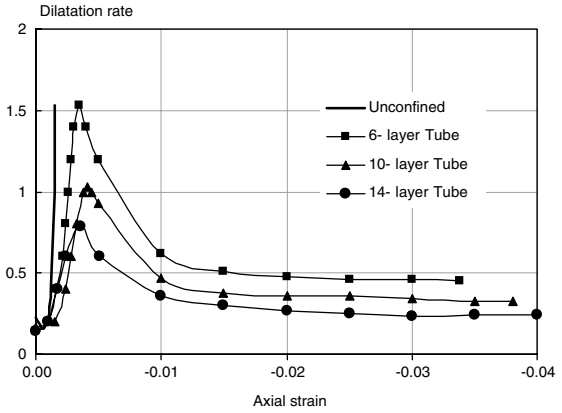

Fig. 8. Dilatational curves for GFRP-encased concrete [13,14].

is clear that with an adequate amount of external fiber composites, lateral expansion of concrete can be effectively avoided.

Fig. 8 shows the dilatational response of FRP-encased concrete that consists of three regions that generally correspond to those already explained for stress–strain curves [13,14]. The initial rate of dilation $\mu = -\frac{d\varepsilon_t}{d\varepsilon_l}$ is the same as the Poisson ratio of unconfined concrete. The dilation rate remains constant during the early stages of loading, when concrete behaves elastically. As severe microcracks develop, the dilatation rate begins to increase. For unconfined concrete, with the growth of cracks opening dilatation becomes unstable. However dilatation of FRP-encased concrete reaches a peak value after which it decreases and finally stabilizes at an asymptotic value.

3. Existing models for confined concrete

The modelling of the behavior of FRP-confined concrete is mostly based on semiempirical equations like that of Samaan et al. [14], which uses a bilinear stress–strain curve and incorporates stiffness of the jacket in calculating lateral strains. The model is shown to work well for concentrically loaded columns [16]. For these models, the stress–strain response provided is strongly dependent on the experimental data used to deduce them. This disadvantage can be overcome by using the theories of elasticity and plasticity as it has been successfully applied in steel confined concrete [4]. This provides a solid theoretical framework to examine concrete columns and gives reasonable predictions.

Recently, Kown et al. [16] developed a hypoelasticity-based concrete model and validated it through correlation studies with experimental tests on concrete cylinders confined by different mechanisms, including steel and fiber reinforced polymer jackets. The model was also applied to the analysis of the three dimensional response of concrete specimens and RC columns. The concrete model is orthotropic, with the axes of orthotropy parallel to the principal stress directions. Principal stress and strain directions are not coaxial. The model is based on the concept of equivalent uniaxial strains. The original model by Balan et al. [8] was modified to include the coupling between the deviatoric and the volumetric stresses. The comparison with experimental results shows good agreement, both in terms of the radial and axial strains and in the prediction of the axial stress at failure, but the complete stress–strain curve is not well reproduced by numerical results neither the dilatational response in the first load stages.

Mirmiran and his co-workers [17,2] developed a nonlinear finite element model with a non-associative Drucker–Prager plasticity to account for restraint pressure sensitivity of concrete. The predicted stress–strain curves are closed to test results. Volumetric expansion tendency of confined concrete, however, is not preserved.

Karabinis and Kiousis [6] modified and calibrated a Drucker–Prager-type constitutive model so as to provide the FRP-confined concrete stress–strain response. In this confinement model concrete responds as an elasto-plastic material following a Drucker–Prager-type [14] hardening–softening criterion. For the analytical model description, 14 material parameters are used to reproduce concrete behavior. From the comparison with experimental results it can be concluded that the model predicts bilinear behavior of the composite system in axial direction but radial and volumetric results are not shown.

Plasticity theory has been used by many authors. Nevertheless, there are many aspects related to the dilation response that are still not well represented. It seems that plasticity theory cannot account for all microstructure changes taking place in confined concrete. An alternative could be the use of theories based on the Disturbed State Concept (DSC) developed by Desai and Zhang [18]. Although this theory has been mainly applied to granular or cohesionless materials, it constitutes a potential tool for the simulation of confined concrete behavior. This theory assumes that applied mechanical and environmental forces cause disturbances or changes in the material microstructure with respect to its behavior under its relative intact (RI) state. The material is initially in a full or a partial RI state, depending upon the initial disturbance. During the deformation the material in the RI state is transformed continuously into the fully adjust (FA) state through a process of natural self-adjustment of its microstructure. At any stage, the material is treated as the mixture of the RI and FA parts, which are distributed (randomly) over the material elements. The observed response of the mixture is expressed in terms of the responses of the materials in the RI and FA states by using the disturbance function,

which can be considered to denote deviation of the observed behavior from those of the two reference states. The behavior of the material in the RI state can be simulated by using a theory based on continuum mechanics such as linear or nonlinear elasticity, elastoplasticity, viscoplasticity or thermoviscoplasticity. The FA state can be represented as (1) the 'failed' material which acts like a 'void' as in the classical damage theory and can carry no stress at all, (2) it can carry hydrostatic stress but no shear stress, like a constrained liquid, or (3) it can continue to carry the shear stress for a given hydrostatic stress, reached up to that point and can deform under constant volume, as in the case of the critical state soil mechanics concept; here, the material acts like a constrained liquid–solid. As the FA material is constrained by the surrounding RI material, the two latter simulations are considered to be more realistic than the first one. At this time, the disturbance, D, is assumed to be a scalar; however, it can be expressed as a tensor. The DSC includes the coupled (observed) response, as it is influenced by the collective behavior of the interacting mechanisms in the RI and FA states.

An alternative to this type of model is a combination of plasticity and damage theories that accounts for the microstructure changes in a phenomenological way.

4. Proposed model

The model presented in this paper is thermodynamically consistent and comes from a generalization of plasticity theory [7,19,20] and isotropic damage theory. The plastic model has been adapted to be able to reproduce the behavior of concrete under triaxial compression. Coupling of damage and plastic strains is achieved by solving both problems simultaneously [7,21]. In this way correct energy dissipation is also assured.

The use of a second degree function in the components of the stress tensor to define the elastic threshold and the ultimate strength allows the accurate reproduction of the variation of ultimate strength with hydrostatic pressure. The hardening variable has also been improved to reproduce energy dissipation in triaxial compression. The reproduction of dilatational response and ductility under high confinement pressure is achieved with the introduction of damage for levels of stress close to the ultimate strength in uniaxial compression.

5. Thermodynamic basis

The constitutive model proposed is based on the hypothesis of *uncoupled elasticity* [22,23]. According to this hypothesis, the total free energy density per unit volume Ψ can be supposed to be formed by two independent parts: an elastic part Ψ^{e} and a plastic part Ψ^{p}, corresponding to the elastic and plastic processes respectively,

$$\Psi(\varepsilon^{\mathrm{e}}_{ij}, \kappa^{\mathrm{p}}, d) = \Psi^{\mathrm{e}}(\varepsilon^{\mathrm{e}}_{ij}, d) + \Psi^{\mathrm{p}}(\kappa^{\mathrm{p}}) \tag{1}$$

where $\varepsilon^{\mathrm{e}}_{ij}$ is the elastic strains tensor, κ^{p} is the plastic hardening variable and d is the damage variable.

For small strains and thermally stable problems, the elastic part of free energy density is written as quadratic function as follows,

$$\begin{aligned}\Psi^{\mathrm{e}}(\varepsilon^{\mathrm{e}}_{ij}, d) &= \frac{1}{2}[\varepsilon^{\mathrm{e}}_{ij} C_{ijkl}(d)\varepsilon^{\mathrm{e}}_{kl}] = \frac{1}{2}[\varepsilon^{\mathrm{e}}_{ij}(1-d)C^{0}_{ijkl}\varepsilon^{\mathrm{e}}_{kl}] \\ &= (1-d)\Psi^{0}(d)\end{aligned} \tag{2}$$

where $C_{ijkl}(d) = (1-d)C^{0}_{ijkl}$ is the secant constitutive tensor affected by the evolution of damage, C^{0}_{ijkl} is the elastic constitutive tensor of the virgin material and Ψ^{0} represents the elastic free energy density for the virgin material. The damage variable d varies from 0, for the undamaged virgin material, to a maximum value $d_{\mathrm{c}} \leqslant 1$, for the completely damaged material, i.e. $0 \leqslant d \leqslant d_{\mathrm{c}}$.

The fulfillment of inequality of Clausius–Planck for a given thermodynamic state is guaranteed if the stress is obtained as follows,

$$\begin{aligned}&\sigma_{ij} = \frac{\partial \Psi^{\mathrm{e}}}{\partial \varepsilon^{\mathrm{e}}_{ij}} = (1-d)\frac{\partial \Psi^{0}}{\partial \varepsilon^{\mathrm{e}}_{ij}} = C_{ijkl}\varepsilon^{\mathrm{e}}_{kl} = (1-d)C^{0}_{ijkl}\varepsilon^{\mathrm{e}}_{kl} \\ &C_{ijkl} = (1-d)C^{0}_{ijkl}; \quad \sigma_{ij} = (1-d)\sigma^{0}_{ij}; \quad \sigma^{0}_{ij} = C^{0}_{ijkl}\varepsilon^{\mathrm{e}}_{kl}\end{aligned} \tag{3}$$

where σ_{ij} is the stress tensor.

Mechanical dissipation must satisfy first inequality of Clausius–Planck and can be decomposed in two parts: one part due to the plastic process $\Xi^{\mathrm{p}}_{\mathrm{m}}$ and the other due to the damage process $\Xi^{\mathrm{d}}_{\mathrm{m}}$,

$$\Xi_m = \underbrace{\sigma_{ij}\dot{\varepsilon}^{\mathrm{p}}_{ij} - \frac{\partial \Psi^{\mathrm{p}}}{\partial \kappa^{\mathrm{p}}}\dot{\kappa}^{\mathrm{p}}}_{\Xi^{\mathrm{p}}_{\mathrm{m}}} \underbrace{- \frac{\partial \Psi^{\mathrm{e}}}{\partial d}\dot{d}}_{\Xi^{\mathrm{d}}_{\mathrm{m}}} \geqslant 0 \tag{4}$$

where $\varepsilon^{\mathrm{p}}_{ij} = \varepsilon_{ij} - \varepsilon^{\mathrm{e}}_{ij}$ is the plastic strain tensor and ε_{ij} is the strain tensor.

5.1. Plastic process

The plastic process is described by a generalization of classical plasticity theory that takes into account many aspects of geomaterials behavior. Elastic threshold is defined by a yield function,

$$F^{\mathrm{p}}(\sigma_{ij}; \kappa^{\mathrm{p}}) = f^{\mathrm{p}}(\sigma_{ij}) - K^{\mathrm{p}}(\sigma_{ij}, \kappa^{\mathrm{p}}) = 0 \tag{5}$$

where $f(\sigma_{ij})$ is the equivalent stress, $K^{\mathrm{p}}(\sigma_{ij}, \kappa^{\mathrm{p}})$ is the yielding threshold and κ^{p} is the plastic hardening variable.

The following rules are used for the evolution of plastic strains $\dot{\varepsilon}^{p}_{ij}$,

$$\dot{\varepsilon}^{p}_{ij} = \dot{\lambda}\frac{\partial G(\sigma_{mn};\kappa^{p})}{\partial \sigma_{ij}} \tag{6}$$

where $\dot{\lambda}$ is the plastic consistency factor and G is the plastic potential function.

The plastic hardening variable κ^{p} is obtained normalizing energy dissipated by the plastic process to unity and varies from 0, for the virgin material, to 1, when the maximum energy is plastically dissipated. The original definition in [7] has been modified to take into account the plastic energy dissipation process under triaxial compression,

$$\begin{aligned}\dot{\kappa}^{p} &= \left[\frac{r}{g_{f}^{*p}} + \frac{(1-r)}{g_{c}^{*p}}\right]\sigma_{ij}\dot{\varepsilon}^{p}_{ij} = \dot{\lambda}h^{p}_{ij}\frac{\partial G}{\partial \sigma_{ij}} \\ h^{p}_{ij} &= \left[\frac{r}{g_{f}^{*p}} + \frac{(1-r)}{g_{c}^{*p}}\right]\sigma_{ij}\end{aligned} \tag{7}$$

where r represents a measure of the ratio between tensile and compressive stresses and can be evaluated as follows,

$$r = \frac{\sum_{i=1}^{3}\langle\sigma_{i}\rangle}{\sum_{i=1}^{3}|\sigma_{i}|} \qquad \langle\sigma_{i}\rangle = \frac{1}{2}[\sigma_{i} + |\sigma_{i}|] \tag{8}$$

σ_{i} are the principal stresses.

$$g_{f}^{*p} = \left(\frac{\sum_{i=1}^{3}|\sigma_{i}|R^{op}}{f^{p}(\sigma_{ij})}\right)^{1+H(-r)} g_{f}^{p}; \quad g_{c}^{*p} = \left(\frac{\sum_{i=1}^{3}|\sigma_{i}|}{f^{p}(\sigma_{ij})}\right) g_{c}^{p} \tag{9}$$

$$H(-r) = \begin{cases} 0 & \text{if } r > 0 \\ 1 & \text{if } r \leqslant 0 \end{cases}$$

R^{op} is the relation between the yielding thresholds in uniaxial compression and that corresponding to uniaxial tension; g_{f}^{p} and g_{c}^{p} are the maximum energy densities dissipated by the plastic process in uniaxial tension and compression processes respectively. In the case of a thermodynamic process with no damage dissipation, they can be evaluated as follows,

$$g_{f}^{p} = \frac{G_{f}}{l_{c}} \quad \text{and} \quad g_{c}^{p} = \frac{G_{c}}{l_{c}} \tag{10}$$

where G_{f} and G_{c} are the fracture and crushing energies respectively [19] and l_{c} is an external parameter that depends on the characteristic size of the finite element mesh that is introduced in order to obtain objectivity of the solid response respect to the mesh size [24].

The original definition of the plastic hardening variable [7,21] was modified by the introduction of an exponent in the terms between brackets in Eq. (9) in order to increase energy dissipation under biaxial and triaxial compression ($r = 0$) according to experimental results.

The following evolution equation is proposed for the equivalent yielding threshold [7,21],

$$K(\sigma_{ij},\kappa^{p}) = r\sigma_{t}(\kappa^{p}) + (1-r)\sigma_{c}(\kappa^{p}), \tag{11}$$

where $\sigma_{t}(\kappa^{p})$ and $\sigma_{c}(\kappa^{p})$ represent the evolution of the yielding threshold in uniaxial tension and compression tests respectively.

Loading/unloading conditions are derived from the Kuhn–Tucker relations formulated for problems with unilateral restrictions,

$$\dot{\lambda} \geqslant 0 \quad F^{p} \leqslant 0 \quad \dot{\lambda}F^{p} = 0 \tag{12}$$

5.2. Damage process

The damage threshold is described by a damage function in the following way [7,21],

$$F^{d} = f^{d}(\sigma_{ij}) - K^{d}(\sigma_{ij},\kappa^{d}) = 0 \tag{13}$$

where $f^{d}(\sigma_{ij})$ is the equivalent tension, $k^{d}(\sigma_{ij},\kappa^{d})$ is the equivalent damage threshold and κ^{d} is the degradation variable.

The equivalent tension $f^{d}(\sigma_{ij})$ can be evaluated using known yielding functions (Tresca, Von Mises, Mohr–Coulomb or Drucker–Prager) or any function specially developed for damage.

The degradation variable κ^{d} varies from 0, for the virgin material, to 1, for the completely damaged material and is obtained normalizing energy dissipated by damage to unity [7,21],

$$\begin{aligned}\dot{\kappa}^{d} &= \left[\frac{r}{g_{f}^{*d}} + \frac{(1-r)}{g_{c}^{*d}}\right]\Psi^{0}\dot{d} = h^{d}\dot{d} \\ h^{d} &= \left[\frac{r}{g_{f}^{*d}} + \frac{(1-r)}{g_{c}^{*d}}\right]\Psi^{0}\end{aligned} \tag{14}$$

$$g_{f}^{*d} = \left(\frac{\sum_{i=1}^{3}|\sigma_{i}|R^{od}}{f^{d}}\right)^{1+H(-r)} g_{f}^{d}; \quad g_{c}^{*d} = \left(\frac{\sum_{i=1}^{3}|\sigma_{i}|}{f^{d}}\right) g_{c}^{d} \tag{15}$$

R^{od} is the relation between the damage thresholds in uniaxial compression and that corresponding to uniaxial tension and g_{f}^{d} and g_{c}^{d} are the maximum energy densities dissipated by damage in uniaxial tension and compression processes respectively [7,21].

As in the case of the plastic hardening variable, an exponent was also introduced in the definition of the damage hardening variable in order to reproduce the experimental results.

The following evolution equation is proposed for the equivalent damage threshold [7,21],

$$K^{d}(\sigma_{ij},\kappa^{d}) = r\sigma_{t}(\kappa^{d}) + (1-r)\sigma_{c}(\kappa^{d}), \tag{16}$$

where $\sigma_{t}(\kappa^{d})$ and $\sigma_{c}(\kappa^{d})$ represent the evolution of the damage threshold in uniaxial tension and compression tests respectively.

The loading/unloading conditions are derived from the Khun–Tucker relations and are analogous to the ones corresponding to the plastic process,

$$\dot{d} \geqslant 0 \quad F^{d} \leqslant 0 \quad \dot{d}F^{d} = 0. \tag{17}$$

5.3. Consistency conditions

Evolution of permanent strains and damage is obtained from the simultaneous solution of the following equations called the *consistency conditions* of the problem,

$$\begin{cases} \dot{F}^{p} = 0 \\ \dot{F}^{d} = 0 \end{cases} \tag{18}$$

Eq. (18) are two linear equations in $\dot{\lambda}$ and $\dot{d}$ that can be easily solved.

5.4. Yielding function

The elastic threshold criterion proposed for concrete is a modification of the Lubliner–Oller [19,25] criterion in order to reproduce the behavior of concrete under high hydrostatic pressures. In order to have curve meridians [26] a second-degree function of the first invariant was introduced,

$$F^{p} = \sqrt{3J_2} + \alpha I_1 + \beta\langle\sigma^{max}\rangle - \gamma\langle-\sigma^{max}\rangle + \frac{\delta}{\sigma_c(\kappa^{p})}(1-\alpha)I_1^2 - \sigma_c(\kappa^{p})(1+\alpha)(1+\delta) \leqslant 0. \tag{19}$$

where α, β, γ and δ are constants that define the shape of the yielding function, I_1 is the first invariant of the stress tensor, J_2 is the second invariant of the deviatoric stress tensor and σ^{max} is the maximum principal stress.

Parameter α takes into account the relation between strength in uniaxial compression f_c' and biaxial compression f_{bc}, $R_{bc} = f_{bc}/f_c'$, see Fig. 9, and it results:

$$\alpha = \frac{R_{bc} + 4\delta R_{bc}^2 - (1+\delta)}{2R_{bc} + 4\delta R_{bc}^2 - (1+\delta)} \tag{20}$$

The shape of the yielding surface on plane $\sigma_2 = 0$ and its comparison with the original surface with straight meridians [19,25] and experimental results by Kupfer et al. [27] are presented in Fig. 9.

Parameter β takes into account the ratio between the strength in uniaxial compression f_c' and uniaxial tension f_t, $R^0 = f_c'/f_t$,

$$\beta = R^0(1-\alpha)(1+\delta) - \frac{\delta}{R^0}(1-\alpha) - (1+\alpha) \tag{21}$$

Parameter γ is a function of the ratio between maximum octahedral radius in compression and tension r_{oct}^{max} and appears only in triaxial stress states, i.e. $\sigma_3 \leqslant \sigma_2 \leqslant \sigma_1 = \sigma^{max} \leqslant 0$. See Fig. 10. For $I_1 = 0$,

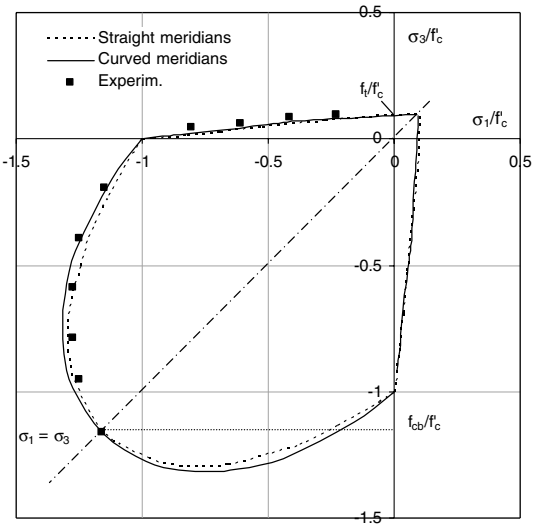

Fig. 9. Proposed yielding surface—plane $\sigma_2 = 0$. Comparison with experimental results [27].

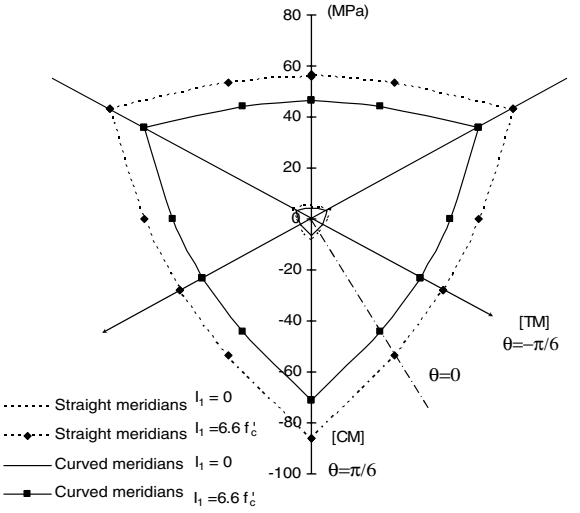

Fig. 10. Proposed yielding surface—octahedral plane.

$$\gamma = \frac{3(1 - r_{oct}^{max})}{2r_{oct}^{max} - 1} \tag{22}$$

The yielding criterion proposed preserves the ratio between octahedral radius constant along the inelastic process and between the range $0.5 \leqslant r_{oct}^{max} \leqslant 1.0$.

Fig. 10 shows the shape of the proposed elastic threshold in octahedral planes corresponding to different octahedral stresses. It is represented by a convex curve with three corners corresponding to the three compression meridian planes.

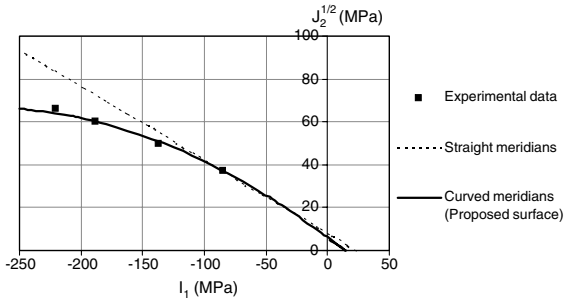

Fig. 11. Comparison of proposed failure surface with triaxial compression experimental results [9].

Parameter $\delta \geqslant 0$ is related to the curvature of the meridians. The shape of the ultimate surface in the compression meridian plane is shown in Fig. 11 together with experimental results [9]. The ultimate surface can be used to define δ. If the compression meridian is forced to pass through the point corresponding to a triaxial compression test with p_h, hydrostatic pressure, and σ_{cu}, compression strength under that confinement, the parameter δ can be evaluated as follows,

$$\delta = -\frac{\sqrt{3J_2}(2R_{bc}-1) + I_1(R_{bc}-1) + \gamma\sigma_{max}(2R_{bc}-1) - \sigma_{cu}R_{bc}}{\sqrt{3J_2}(4R_{bc}^2-1) + I_1\left(4R_{bc}^2 - 1 + \frac{R_{bc}}{\sigma_{cu}}I_1\right) + \gamma\sigma_{max}(4R_{bc}^2-1) - \sigma_{cu}R_{bc}}$$
$$J_2 = \frac{(p_h - \sigma_{cu})^2}{3}, \quad I_1 = \sigma_{cu} + 2p_h \tag{23}$$

For $\delta = 0$ the original yielding criterion of Lubliner–Oller [25] with straight meridians is recovered.

The same value of parameter δ obtained for the ultimate strength can be used for the elastic threshold. As a result, the curve describing the initial elastic threshold has more curvature than that defining the ultimate strength. This fact is in accordance with experimental results which show that the difference between the elastic limit and the ultimate strength grows with hydrostatic pressure. See Fig. 12.

The function described by Eq. (19), with curve meridians, can also be used as a plastic potential function to control dilatancy for high confinement pressures.

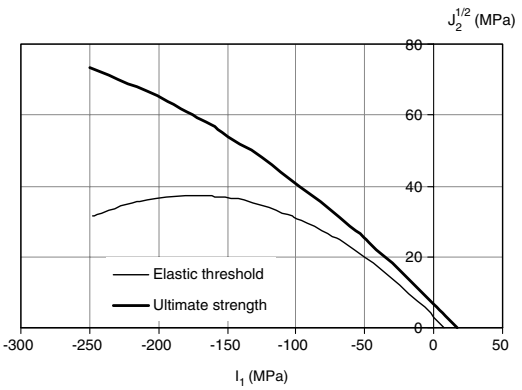

Fig. 12. Proposed yielding and ultimate strength surfaces—compression meridian plane.

6. Model parameters

The model proposed includes many parameters because it has been conceived as a general model that can be calibrated for different types of materials by setting appropriate values for the parameters. Nevertheless, as the paper is focused on the application to concrete, some guides on how to obtain the parameters are given below.

Basically, the following data are required to completely define the proposed constitutive model for a specific material:

Functions:

(a) Yielding function: The proposed yielding function can be used for concrete.
(b) Plastic potential function: The proposed yielding function can be used as plastic potential function for concrete.
(c) Damage function: A Von Mises function can be used to describe damage due to changes in porous structure of concrete taking place under high confining pressures.

Data:

(a) Elastic properties
Elasticity modulus and Poisson's ratio of concrete can be obtained from a uniaxial compression test. Nevertheless, there are many empirical equations that could be used for the estimation of the elastic modulus as a function of the compressive strength f'_c, in case the stress–strain curve for the uniaxial test is not available. As an example, the following

expression proposed by Ahmad and Shah [28] can be used,

$$E_1 = 3950\sqrt{f'_c}\ [\text{MPa}] \tag{24}$$

Poisson's ratio of concrete normally ranges from 0.15 to 0.22 [26,27,29], it is lower under tension stresses than under compression stresses. It can be approximate as 0.19 or 0.20 [19].

(b) Compression strength f'_c
The compression strength strongly depends on the type of concrete and the model cannot be calibrated without this value.

(c) Compression elastic limit
The compression elastic limit can be obtained from the stress–strain curve of a uniaxial compression test. Although linear elastic limit correspond to approximately 0.30–0.40f'_c [27], for the sake of simplicity, the behavior can be supposed to be elastic up to the discontinuity level [29] that represents the onset of major microcracking. For uniaxial compression tests, this discontinuity is defined as the point at which Poisson's ratio begins to increase and occurs at about 75% of the ultimate strength [19].

(d) Plastic damage variable for the peak stress $\kappa^{\text{p}}_{\text{comp}}$.
It can be obtained from a uniaxial compression stress–strain curve but it always ranges from 0.1 to 0.20.

(e) Compression/tension strength ratio, $R^0 = f'_c/f_t$
This value can be obtained if uniaxial compression and tension strengths are available. According to experimental results [27], the value of R^0 is 9.1, 11.1 and 12.5 for compressive strengths of 19, 32 and 60 MPa respectively and can be approximate as 10 for a normal strength concrete.

(f) Biaxial compression/uniaxial compression strength ratio $R_{\text{bc}} = f_{\text{bc}}/f'_c$
This value can be obtained from biaxial tests [27] and it ranges from 1.10 to 1.16.

(g) Ratio between maximum octahedral radius in compression and tension $r^{\max}_{\text{oct}}$
Experimental results indicate that $r^{\max}_{\text{oct}}$ tends to a constant value of about 0.65, from which results $\gamma = 3.5$ [19,25].

(h) Compression meridians curvature
It is defined by a point corresponding to a triaxial compression test, with p_h, hydrostatic pressure, and σ_{cu}, compression strength under that confinement. If these results are not available, there are many empirical equations for the prediction of compressive strength as a function of confinement pressure [9]. From the experimental results used in the application examples presented later, the following expressions can be used for the estimation of that point for normal and high-strength concrete respectively,

Normal strength concrete [30],

$$\frac{\sigma_{cu}}{f'_c} = 1 + 3.5\left(\frac{p_h}{f'_c}\right)^{0.85} \tag{25}$$

High-strength concrete [31],

$$\frac{\sigma_{cu}}{f'_c} = -1.228 + 2.172\left(1 + 7.46\frac{p_h}{f'_c}\right)^{0.5} - 2\frac{p_h}{f'_c} \tag{26}$$

(i) Fracture and crushing energy
Fracture energy of concrete can be obtained from three point bend tests on notched beams [32]. It ranges from 150 to 300 Pa m [19]. Crushing energy [19] can be approximated as $G_c \approx (R^0)^2 G_f$.

(j) Damage threshold in uniaxial compression
It can be obtained from a cyclic compression test but, according with application examples presented later, it can be approximately taken as $0.90f'_c$.

(k) Damage hardening curve $\sigma_c(\kappa^{\text{d}})$ can be obtained from uniaxial cyclic tests but it can be approximated as linear with a slope equal to 0.012 to 0.015.

7. Algorithm for the numerical integration

For the proposed model, yielding and damage equations must be integrated simultaneously. The Euler-Backward algorithm presented in Table 1 is used for this purpose [7]. Between two equilibrium configurations n and $n-1$ the variables of the problem are updated as follows:

$$(\varepsilon^{\text{p}}_{ij})_n = (\varepsilon^{\text{p}}_{ij})_{n-1} + \Delta\lambda_n\left(\frac{\partial G}{\partial \sigma_{ij}}\right)_n \tag{27}$$

$$(\kappa^{\text{p}})_n = (\kappa^{\text{p}})_{n-1} + \Delta\lambda_n (h^{\text{p}}_{ij})_n\left(\frac{\partial G}{\partial \sigma_{ij}}\right)_n \tag{28}$$

$$d_n = d_{n-1} + \Delta d_n \tag{29}$$

$$(\sigma_{ij})_n = (1 - d_n)C^0_{ijkl}[(\varepsilon_{kl})_n - (\varepsilon^{\text{p}}_{kl})_n] \tag{30}$$

Replacing these equations in Eqs. (5) and (13), corresponding to yielding and damage conditions, the following nonlinear system of equations is obtained,

$$\begin{cases} H^{\text{p}}(\Delta\lambda_n, \Delta d_n) = F^{\text{p}}[(\sigma_{ij})_n; (k^{\text{p}})_n] = 0 \\ H^{\text{d}}(\Delta\lambda_n, \Delta d_n) = F^{\text{d}}[(\sigma_{ij})_n; (k^{\text{d}})_n] = 0 \end{cases} \tag{31}$$

This system can be solved, for example, by the Newton–Raphson method, between to iteration $k-1$ and k, the variable are updated as follows (Table 1):

$$\begin{Bmatrix} \Delta\lambda_n \\ \Delta d_n \end{Bmatrix}_k = \begin{Bmatrix} \Delta\lambda_n \\ \Delta d_n \end{Bmatrix}_{k-1} - \begin{bmatrix} \left(\frac{\partial H^{\text{p}}}{\partial \Delta\lambda}\right)_n & \left(\frac{\partial H^{\text{p}}}{\partial \Delta d}\right)_n \\ \left(\frac{\partial H^{\text{d}}}{\partial \Delta\lambda}\right)_n & \left(\frac{\partial H^{\text{d}}}{\partial \Delta d}\right)_n \end{bmatrix}^{-1}_{k-1} \times \begin{Bmatrix} H^{\text{p}}(\Delta\lambda_n, \Delta d_n) \\ H^{\text{d}}(\Delta\lambda_n, \Delta d_n) \end{Bmatrix}^{k-1} \tag{32}$$

Table 1
Algorithm for the numerical integration of constitutive equations [7]

(1) Initialization: $k = 0; \Delta\lambda_n^0 = 0; \Delta d_n^0 = 0$
(2) $k = k + 1$
(3) Plastic strain updating: $(\varepsilon_{ij}^{\mathrm{p}})_n^k = (\varepsilon_{ij}^{\mathrm{p}})_{n-1} + \Delta\lambda_n^{k-1}(\frac{\partial G}{\partial \sigma_{ij}})_n^{k-1}$
(4) Damage variable updating: $d_n^k = d_{n-1} + \Delta d_n^{k-1}$
(5) Non damaged stress updating: $(\sigma_{ij}^0)_n^k = C_{ijkl}^0[(\varepsilon_{kl})_n - (\varepsilon_{kl}^{\mathrm{p}})_n^k]$
(6) Damaged stress updating: $(\sigma_{ij})_n^k = (1 - d_n^k)(\sigma_{ij}^0)_n^k$
(7) Updating of the other internal variables: $(\kappa^{\mathrm{p}})_n^k = (\kappa^{\mathrm{p}})_{n-1} + \Delta\lambda_n^k (h_{ij}^{\mathrm{p}})_n^k \left(\frac{\partial G}{\partial \sigma_{ij}}\right)_n^k, \quad (\kappa^{\mathrm{d}})_n^k = (\kappa^{\mathrm{d}})_{n-1} + (h^{\mathrm{d}})_n^k \Delta d_n^k$
(8) Yielding and damage conditions: If $(H^{\mathrm{p}})_n^k \leqslant 0$ and $(H^{\mathrm{d}})_n^k \leqslant 0$ goto (14)
(9) If $(H^{\mathrm{p}})_n^k \geqslant 0$ goto (11)
(10) $(\partial H^{\mathrm{p}}/\partial \Delta d)_n^k = 0$ goto (13)
(11) If $(H^{\mathrm{d}})_n^k \geqslant 0$ goto (13)
(12) $(\partial H^{\mathrm{d}}/\partial \Delta\lambda)_n^k = 0$
(13) $\Delta\lambda_n^{k+1} = \Delta\lambda_n^k - \dfrac{\langle H^{\mathrm{p}}(\Delta\lambda_n^k, \Delta d_n^k)\rangle (\partial H^{\mathrm{d}}/\partial \Delta d)_n^k - \langle H^{\mathrm{d}}(\Delta\lambda_n^k, \Delta d_n^k)\rangle (\partial H^{\mathrm{p}}/\partial \Delta d)_n^k}{(\partial H^{\mathrm{p}}/\partial \Delta\lambda)_n^k (\partial H^{\mathrm{d}}/\partial \Delta d)_n^k - (\partial H^{\mathrm{d}}/\partial \Delta\lambda)_n^k (\partial H^{\mathrm{p}}/\partial \Delta d)_n^k}$

$\Delta d_n^{k+1} = \Delta d_n^k - \dfrac{\langle H^{\mathrm{d}}(\Delta\lambda_n^k, \Delta d_n^k)\rangle (\partial H^{\mathrm{p}}/\partial \Delta\lambda)_n^k - \langle H^{\mathrm{p}}(\Delta\lambda_n^k, \Delta d_n^k)\rangle (\partial H^{\mathrm{d}}/\partial \Delta\lambda)_n^k}{(\partial H^{\mathrm{p}}/\partial \Delta\lambda)_n^k (\partial H^{\mathrm{d}}/\partial \Delta d)_n^k - (\partial H^{\mathrm{d}}/\partial \Delta\lambda)_n^k (\partial H^{\mathrm{p}}/\partial \Delta d)_n^k}$

Goto (2)
(14) $(\varepsilon_{ij}^{\mathrm{p}})_n = (\varepsilon_{ij}^{\mathrm{p}})_n^k; (\kappa^{\mathrm{p}})_n = (\kappa^{\mathrm{p}})_n^k; d_n = d_n^k; (\kappa^{\mathrm{d}})_n = (\kappa^{\mathrm{d}})_n^k; (\sigma_{ij})_n = (\sigma_{ij})_n^k$
(15) END

The incremental stress–strain relation can be summarized as [7]:

$$(\Delta\sigma_{ij})_n = \left(\widehat{C}_{ijkl}\right)_n (\Delta\varepsilon_{ij})_n \tag{33}$$

where $\hat{C}_{ijkl}$ is the consistent tangent modulus [7],

$$(\widehat{C}_{ijkl})_n = (C_{ijkl}^{\mathrm{e}*})_n - \frac{(C_{ijpq}^*)_n \left(\frac{\partial G}{\partial \sigma_{pq}}\right)_n \left(\frac{\partial F^{\mathrm{p}}}{\partial \sigma_{rs}}\right)_n (C_{rskl}^{\mathrm{e}*})_n}{-\left(\frac{\partial F^{\mathrm{p}}}{\partial \kappa^{\mathrm{p}}}\right)_n (h_{tu}^{\mathrm{p}})_n \left(\frac{\partial G}{\partial \sigma_{tu}}\right)_n + \left(\frac{\partial F^{\mathrm{p}}}{\partial \sigma_{pq}}\right)_n (C_{pqrs}^*)_n \left(\frac{\partial G}{\partial \sigma_{rs}}\right)_n} \tag{34}$$

$$(C_{ijkl}^*) = \left[\delta_{ip}\delta_{jq} + \Delta\lambda_n (C_{ijrs})_n \left(\frac{\partial^2 G}{\partial \sigma_{rs}\partial \sigma_{pq}}\right)_n\right]^{-1} C_{pqkl} \tag{35}$$

$$(C_{ijkl}^{\mathrm{e}*}) = \left[\delta_{ip}\delta_{jq} + \Delta\lambda_n (C_{ijrs})_n \left(\frac{\partial^2 G}{\partial \sigma_{rs}\partial \sigma_{pq}}\right)_n\right]^{-1} C_{pqkl}^{\mathrm{e}} \tag{36}$$

8. Comparison with experimental results

8.1. Uniaxial compression

First the behavior of cylindrical concrete specimens of two different strengths (H30 and H70) under uniaxial compression was studied with the proposed model and compared with experimental results [9]. Concrete was modelled as an elastoplastic damaged material with the mechanical properties presented in Table 2. Only one quarter of the cylindrical specimen that has 30 cm height and 15 cm diameter was modelled with one axial symmetric finite element.

Figs. 13 and 14 show the axial stress–axial and transverse strain curves obtained for both types of concrete and their comparison with experimental results. Numerical and experimental volumetric responses are also compared in Figs. 13 and 14. A good agreement between numerical and experimental results can be observed, not only in axial but also in transverse direction.

It may be observed that the behavior under uniaxial compression is almost not modified by damage. Initial stiffness is preserved.

$$C_{ijkl}^{\mathrm{e}} = C_{ijkl} - \frac{\sigma_{ij}^0 \left[\frac{\partial F^{\mathrm{d}}}{\partial \sigma_{tu}}\left(-\frac{\partial F^{\mathrm{p}}}{\partial \kappa^{\mathrm{p}}} h_{mn}^{\mathrm{p}} \frac{\partial G}{\partial \sigma_{mn}} + \frac{\partial F^{\mathrm{p}}}{\partial \sigma_{mn}} C_{mnrs} \frac{\partial G}{\partial \sigma_{rs}}\right) - \left(\frac{\partial F^{\mathrm{d}}}{\partial \sigma_{mn}} C_{mnrs} \frac{\partial G}{\partial \sigma_{rs}}\right) \frac{\partial F^{\mathrm{p}}}{\partial \sigma_{tu}}\right] C_{tukl}}{\left(-\frac{\partial F^{\mathrm{p}}}{\partial \kappa^{\mathrm{p}}} h_{mn}^{\mathrm{p}} \frac{\partial G}{\partial \sigma_{mn}} + \frac{\partial F^{\mathrm{p}}}{\partial \sigma_{mn}} C_{mnrs} \frac{\partial G}{\partial \sigma_{rs}}\right)\left(-\frac{\partial F^{\mathrm{d}}}{\partial \kappa^{\mathrm{d}}} h^{\mathrm{d}} + \frac{\partial F^{\mathrm{d}}}{\partial \sigma_{tu}} \sigma_{tu}^0\right) - \left(\frac{\partial F^{\mathrm{p}}}{\partial \sigma_{mn}} C_{mnrs} \frac{\partial G}{\partial \sigma_{rs}}\right) \frac{\partial F^{\mathrm{p}}}{\partial \sigma_{tu}} \sigma_{tu}^0} \tag{37}$$

Table 2
Mechanical properties of concrete (confined compression tests [9])

Property	H30	H70
Elasticity modulus, E	23800 MPa	33700 MPa
Poisson's ratio, ν	0.2	0.2
Compression ultimate strength, f'_c	33.2 MPa	67 MPa
Uniaxial compression elastic threshold, σ_{fc}	20 MPa	45 MPa
Elastic threshold ratio, R_0^p	10	10
R_{bc}	1.16	1.16
γ	3	3
Confined compression		
p_h	35 MPa	50 MPa
σ_{ccu}	144 MPa	200 MPa
Plastic damage variable for the peak stress, κ_{comp}^p	0.15	0.15
Crushing energy, G_c^p	1.55E−2 MPa m	1.9E−2 MPa m
Fracture energy, G_f^p	1.55E−4 MPa m	1.9E−4 MPa m
Uniaxial compression damage threshold, σ_c^d	30 MPa	65 MPa
Damage hardening slope	300 MPa	500 MPa

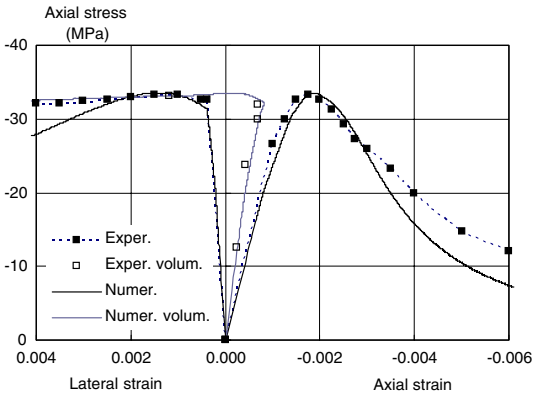

Fig. 13. Stress–strain curves for H30 concrete under uniaxial compression. Comparison with experimental results [9].

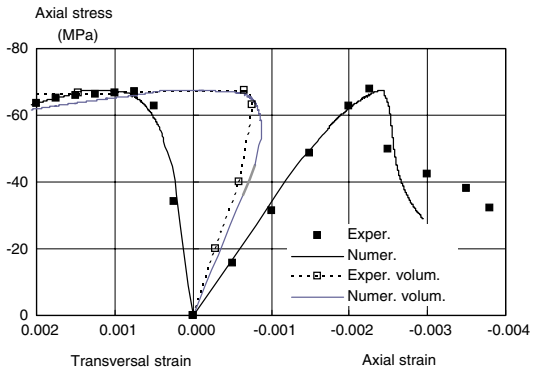

Fig. 14. Stress–strain curves for H70 concrete under uniaxial compression [9]. Comparison with experimental results [9].

8.2. Biaxial tension

Biaxial tests of plane square concrete specimens tested by Kupfer et al. [27] are reproduced in this section. Mechanical properties of concrete are presented in Table 3. The specimens are tested under uniaxial tension, biaxial symmetric tension and biaxial tension with a ratio of principal stress of 1/0.55. The stress–strain curves in principal directions for the three tests are presented in Fig. 15. A good agreement with experimental results is obtained. Both strength and ductility under different stress ratio are well reproduced.

Table 3
Mechanical properties of concrete (biaxial tension tests [27])

Property	
Elasticity modulus, E	22900 MPa
Poisson's ratio, ν	0.18
Compression ultimate strength, f'_c	29.5 MPa
Uniaxial compression elastic threshold, σ_{fc}	22.9 MPa
Elastic threshold ratio, R_0^p	10
R_{bc}	1.16
γ	3
Confined compression	
p_h	30 MPa
σ_{ccu}	125 MPa
Plastic damage variable for the peak stress, κ_{comp}^p	0.15
Crushing energy, G_c^p	1.3E−2 MPa m
Fracture energy, G_f^p	1.3E−4 MPa m
Uniaxial compression damage threshold, σ_c^d	27 MPa
Damage hardening slope	300 MPa

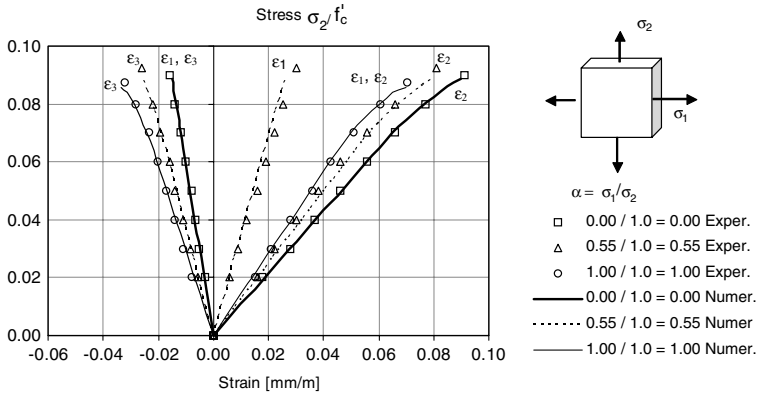

Fig. 15. Stress–strain curves for concrete under biaxial tension. Comparison with experimental results [27].

8.3. Confined compression

Triaxial compression tests of cylindrical concrete specimens are reproduced in this section [9]. The first tests simulated correspond to concretes H30 and H70 of Table 2. First the specimens were subject to a hydrostatic pressure. Then, the lateral confinement was kept constant and the axial stress was incremented until failure. The corresponding axial stress–axial strain curves for both types of concrete and different confinement pressures are presented in Figs. 16 and 17. It can be observed that numerical results approximately reproduce experimental results. Not only the variation of ultimate strength but also the ductility under high confinement

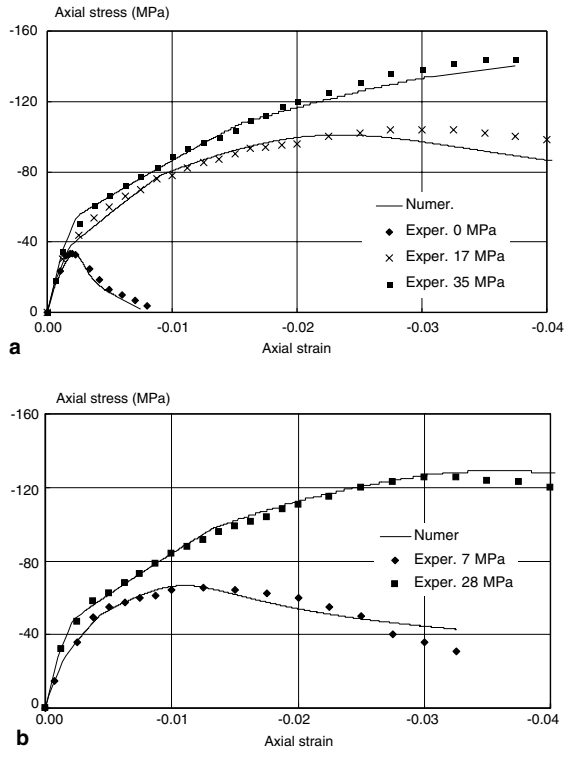

Fig. 16. Stress–strain curves for compression tests under different confinement pressures, normal strength concrete H30. Comparison with experimental results [9]. (a) p = 0–17–35 MPa; (b) p = 7–28 MPa.

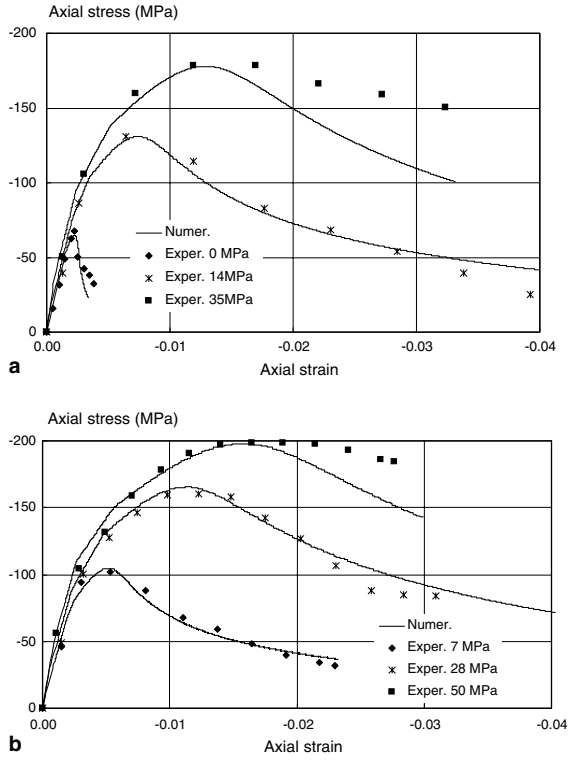

Fig. 17. Stress–strain curves for compression tests under different confinement pressures, high-strength concrete H70. Comparison with experimental results [9]. (a) p = 0–14–35 MPa; (b) p = 7–28–50 MPa.

pressures are reproduced. Many attempts to use classical plasticity models for concrete have failed because they conducted to more brittle stress–strain curves. The shape of the elastic threshold function in combination with the introduction of damage gives a more gradually loss of tangent stiffness prior to the attainment of maximum strength.

Additionally, other group of compression tests confined with hydrostatic pressure are reproduced [12]. The corresponding mechanical properties are presented in Table 4. Fig. 18 shows the variation of axial strains and transverse strains with axial stress for different confinement pressures. It can be observed that a reasonable agreement is found between numerical and experimental results, not only in axial but also in radial direction. The introduction of damage before plastic threshold for high confinement pressures leads to ductile behavior in axial direction with non-dilatational effect. Moreover, the use of plastic potential function with curve meridians as that described by Eq. (19) and represented in Fig. 11, gives a plastic flow with reduced volumetric component. Nevertheless, it may be observed that the estimation of ultimate strength is not so accurate as for those results shown in Figs. 16 and 17. The differences observed in this case are due to the fact that the ultimate

Table 4
Mechanical properties of concrete (confined compression tests [12])

Property	H30
Elasticity modulus, E	26 600 MPa
Poisson's ratio, ν	0.2
Compression ultimate strength, f'_c	32.8 MPa
Uniaxial compression elastic threshold, σ_{fc}	20 MPa
Elastic threshold ratio, R_0^p	10
R_{bc}	1.16
γ	3
Confined compression	
p_h	30 MPa
σ_{ccu}	125 MPa
Plastic damage variable for the peak stress, κ_{comp}^p	0.15
Crushing energy, G_c^p	1.6E−2 MPa m
Fracture energy, G_f^p	1.6E−4 MPa m
Uniaxial compression damage threshold, σ_c^d	30 MPa
Damage hardening slope	225 MPa

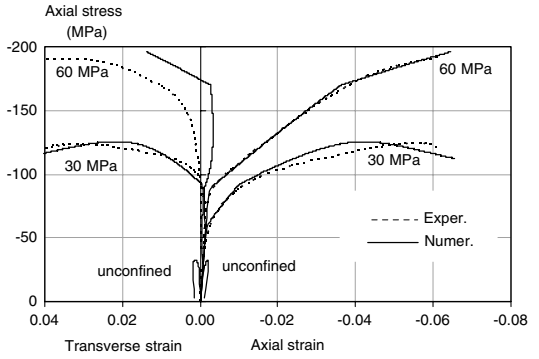

Fig. 18. Axial stress vs axial and lateral strain curves for compression tests under different confinement pressures, $p = 0$–30–60 MPa. Comparison with experimental results [12].

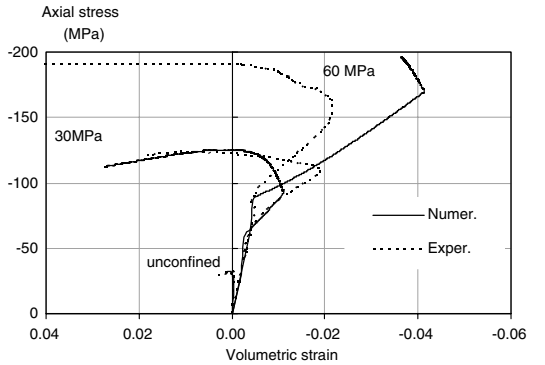

Fig. 19. Evolution of volumetric strains for compression tests with different confinement pressures, $p = 0$–30–60 MPa. Comparison with experimental results [12].

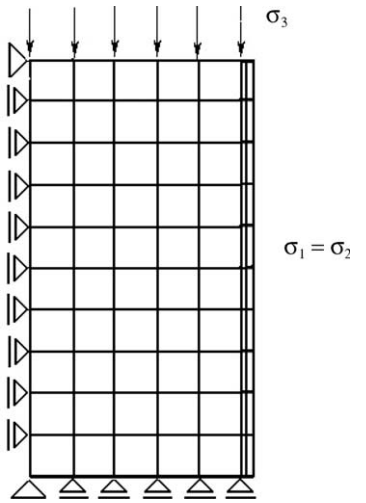

Fig. 20. Finite element mesh for cylindrical concrete specimens confined with steel tubes.

Table 5
Mechanical properties of steel [9]

Elasticity model, E	200 000 MPa
Poisson's ratio, ν	0.3
Yielding stress, σ_f	355 MPa
Yielding function	Von Mises
Plastic potential function	Von Mises

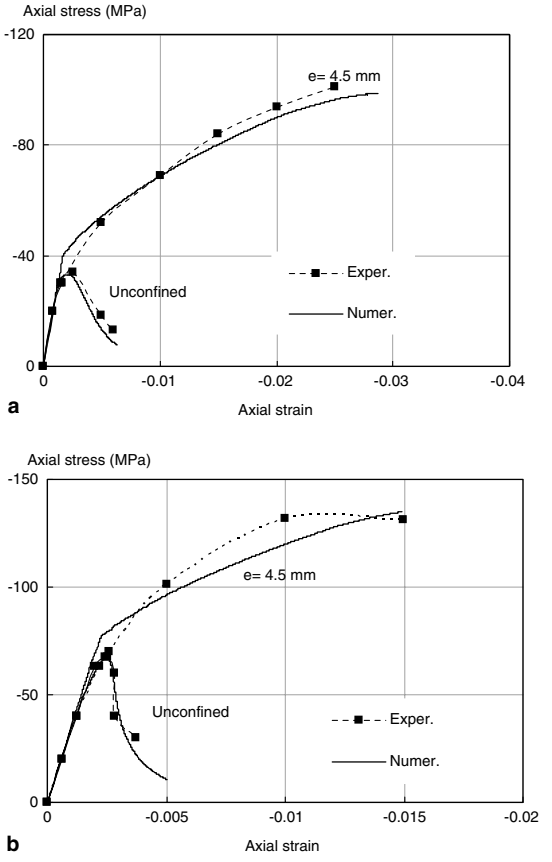

Fig. 21. Stress vs strain curves for compression tests of concrete specimens confined with steel tubes. Comparison with experimental results [9]. (a) Normal strength concrete H30; (b) high-strength concrete H70.

Table 6
Mechanical properties of concrete confined with fiber composites [9]

Property	H30F
Elasticity modulus, E	25000 MPa
Poisson's ratio, ν	0.2
Compression ultimate strength, f_c'	42 MPa
Uniaxial compression elastic threshold, σ_{fc}	20 MPa
Elastic threshold ratio, R_0^p	10
R_{bc}	1.16
γ	3
Confined compression	
p_h	35 MPa
σ_{ccu}	151 MPa
Plastic damage variable for the peak stress, κ_{comp}^p	0.15
Crushing energy, G_c^p	2.0E−2 MPa m
Fracture energy, G_f^p	2.0E−4 MPa m
Uniaxial compression damage threshold, σ_c^d	40 MPa
Damage hardening slope	400 MPa

Table 7
Mechanical properties of CFRP [9]

Longitudinal elasticity modulus, E_l	200000 MPa
Transversal elasticity modulus, E_t	26100 MPa
Longitudinal–transversal Poisson's ratio, ν_{lt}	0.26
Transversal–longitudinal Poisson's ratio, ν_{tl}	0.037
Transversal–transversal Poisson's ratio, ν_{tt}	0.35
Longitudinal tensile strength, σ_{long}^u	2700 MPa
Transverse tensile strength, σ_t^u	54 MPa
Layer thickness	0.117 mm

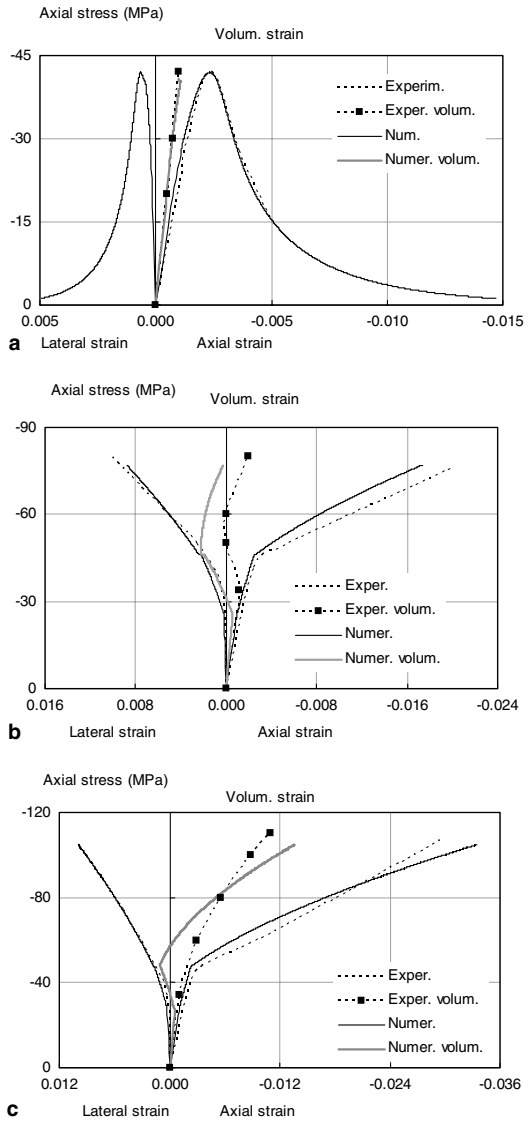

Fig. 22. Stress–strain and volumetric responses of CFRP-confined concrete H30F. Comparison with experimental results [9]. (a) Unconfined; (b) confined with 3 CFRP layers; (c) confined with 6 CFRP layers.

Table 8
Mechanical properties of concrete [13]

Elasticity modulus, E	23273 MPa
Poisson's ratio, v	0.2
Compression ultimate strength, f'_c	31 MPa
Uniaxial compression elastic threshold, σ_{fc}	28 MPa
Elastic threshold ratio, R_0^p	8
R_{bc}	1.16
γ	3
Confined compression	
p_h	30 MPa
σ_{ccu}	120 MPa
Plastic damage variable for the peak stress, κ_{comp}^p	0.15
Crushing energy, G_c^p	1.5E−2 MPa m
Fracture energy, G_f^p	1.5E−4 MPa m
Uniaxial compression damage threshold, σ_c^d	30 MPa
Damage hardening slope	190 MPa

Table 9
Mechanical properties of GFRP [13]

Longitudinal elasticity modulus, E_l	37233 MPa
Transversal elasticity modulus, E_t	12400 MPa
Longitudinal–transversal Poisson's ratio, v_{lt}	0.26
Transversal–longitudinal Poisson's ratio, v_{tl}	0.1
Transversal–transversal Poisson's ratio, v_{tt}	0.29
Circumferential tensile strength, σ_{long}^u	524 MPa
Layer thickness	0.21 mm

plastic surface is simulated with a second-degree polynomial that is not able to exactly adjust all experimental results in a such a wide range of hydrostatic pressures, from 0 to twice the uniaxial compression strength. More accurate results could be obtained with higher degree polynomials.

The evolution of the volumetric strains and the dilatational rate for different confinement pressures are represented and compared with experimental results in Fig. 19. It can be observed that numerical results follow the same tendency that experimental ones.

8.4. Confinement with steel tubes

The behavior of cylindrical concrete specimens confined with steel tubes is represented in this section [9].

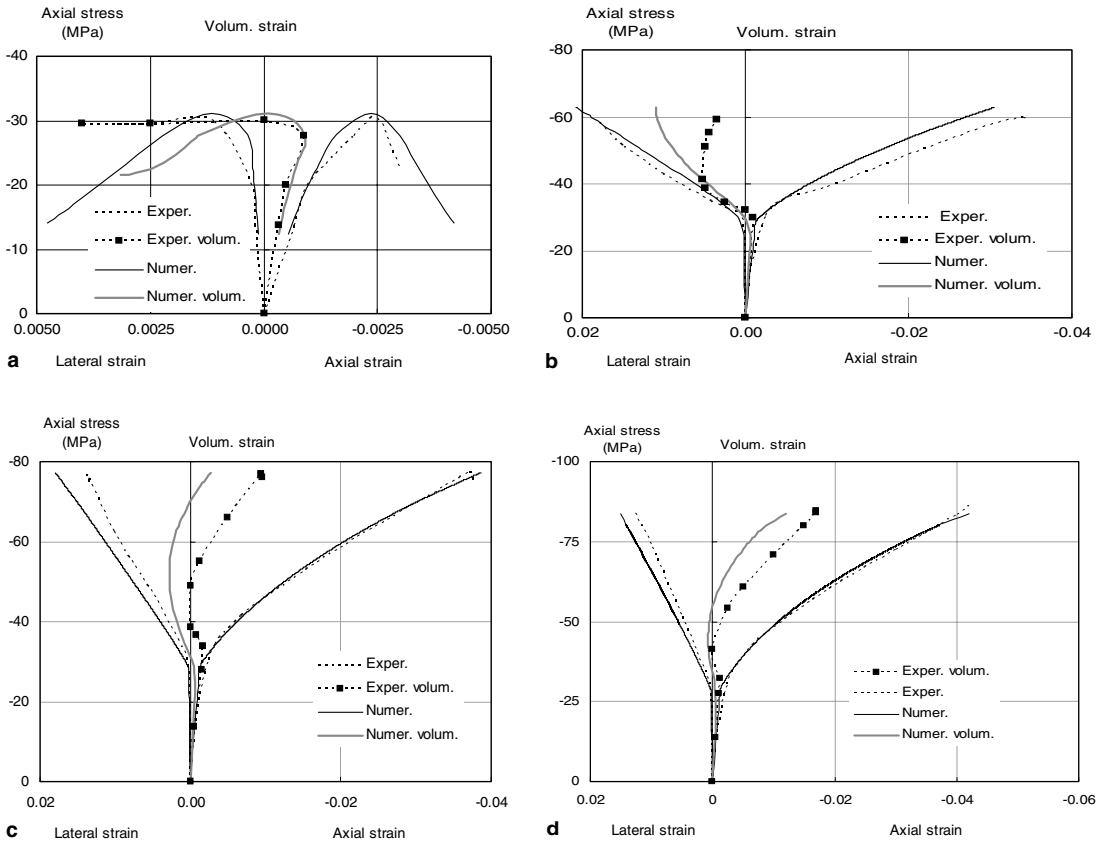

Fig. 23. Stress–strain and volumetric responses of GFRP confined concrete. Comparison with experimental results [13]. (a) Unconfined; (b) confined with 6 GFRP layers; (c) confined with 10 GFRP layers; (d) 14 GFRP layers.

The mechanical properties of concrete are the same as those presented in Table 2. The steel tube is 4.5 mm thick in both cases. In the tests the load is applied only on the concrete core.

Fig. 20 shows the finite element mesh used for both problems. Lubrication between the concrete core and the steel cylinder is explicitly modelled through a very thin layer of axial symmetric elements. As an approximation, this lubrication layer is supposed to be elastic, almost incompressible, but with a very low shear stiffness in order to allow the relative displacement of the concrete core from the steel tube.

Steel is modelled as an elastic-perfectly plastic material with the mechanical properties presented in Table 5.

The stress–strain curves obtained for both types of concrete are presented in Fig. 21. A good agreement between numerical and experimental results is found for concrete with steel confinement.

8.5. FRP confinement

The behavior of cylindrical concrete specimens confined with FRP composites is analyzed in this section.

First the behavior of concrete H30F confined with a carbon fiber reinforced composite with epoxy matrix is simulated [9]. Specimens confined with different number of confinement layers are tested under compression. The mechanical properties of concrete H30F are slightly different from those in Table 2 and are condensed in Table 6. The composite is modelled as an elastic brittle orthotropic material with the mechanical properties presented in Table 7.

Fig. 22 shows the stress–strain and volumetric responses of FRP confined concrete for different number of confinement layers. It can be seen that a good agreement between numerical and experimental results is obtained. With a proper number of composite layers, the dilatational response of plain concrete can be compensated and also reversed. For this case the volumetric response is always a contraction.

Cylindrical (152.5×305 mm) concrete-filled GFRP tubes were also analyzed [13]. The mechanical properties of concrete are condensed in Table 8. FRP tubes consist of a filament-wound angle ply of polyester resin with unidirectional E-Glass fibers at ±15° winding angle. Three distinct jackets thicknesses of 6, 10 and 14 plies (layers) were tested. The thickness, hoop strength and modulus of elasticity of the FRP tubes are presented in Table 9.

Stress–strain curves and volumetric response obtained for plain concrete and the three types of FRP

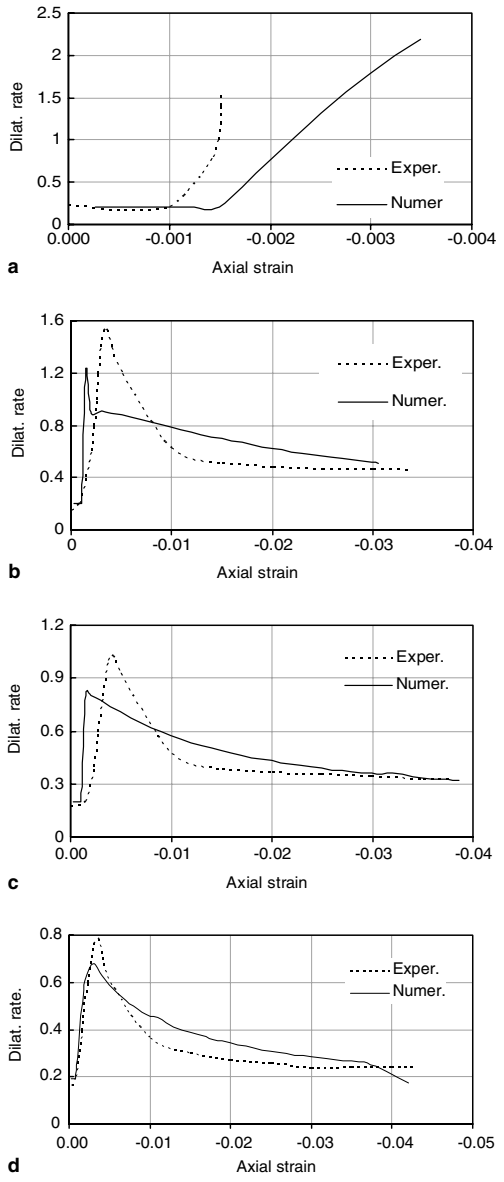

Fig. 24. Dilatation ratio curves for GFRP-confined concrete. Comparison with experimental results [13]. (a) Unconfined; (b) confined with 6 GFRP layers; (c) confined with 10 GFRP layers; (d) confined with 14 GFRP layers.

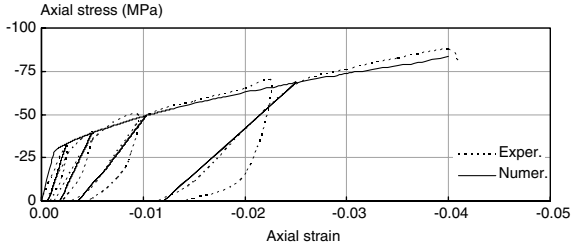

Fig. 25. Uniaxial cyclic response of GFRP-encased concrete under compression. Comparison with experimental results [13].

tubes are plotted in Fig. 23 together with experimental results corresponding to batch C [13]. The predicted response matches experimental results in all cases. Fig. 24 shows the dilatation response curves for plain concrete and for the different thickness of FRP confinement. Numerical results show the same variation than experimental ones in all cases. Dilatational effect is reversed by the confinement and the dilatation rate reaches a maximum, then decreases and finally stabilizes at an asymptotic value.

To evaluate the stiffness degradation and compare it with experimental results a cyclic compression test of the 14-layer specimen (DA32) was reproduced. The specimen was subjected to four unloading-reloading cycles. The stress–strain response obtained with the proposed model and that recorded in the test are plotted in Fig. 25. It can be concluded that, although the numerical model is not able to reproduce the loops registered in the tests, it accurately reproduces the average stiffness degradation due to damage.

9. Conclusions

The plastic damage model presented accurately reproduces the behavior of confined concrete, not only in the axial direction but also in the transverse one.

The adequate computation of transverse strains in confined concrete columns plays a crucial role in the evaluation of the FRP retrofitting system. FRP behaves elastically, so the confinement pressure is always increasing until the tensile failure of the FRP layers. As the stress state in the composite mainly depends on the transverse deformation of the concrete core, it might be properly evaluated in order to predict the ultimate load capacity of the retrofitted column.

Although the model involves a considerable number of material parameters, most of them can be obtained from stress–strain curves in uniaxial tension and compression tests or can be evaluated using empirical expressions because they take values that can be easily identified with the compression strength of concrete. The consideration of damage requires additional data about the stiffness degradation that can be obtained from cyclic tests but can be approximated from the concrete quality.

The numerical response obtained with the plastic damage model is closer to experimental results than that obtained with a plastic model with the same yielding function and hardening variable. The difference between the two types of models is more marked in the case of triaxial compression.

While permanent strains can be associated with the development of microcracks, damage is due to changes in the pore structure of concrete. There is experimental evidence regarding concrete stiffness degradation under triaxial compression. This stiffness degradation is one of the manifestations of damage due to the destruction of pore structure as a result of high pressures.

On the other side, if the tangent stiffness loose in a confined compression test is attributed to damage, a marked nonlinearity in the axial direction, without the classical dilatancy of plastic models, can be obtained for compression stresses lower than the peak one. In this way, the consideration of damage allows not only to reproduce stiffness degradation but also the transverse and volumetric response.

The modification of the plastic hardening variable proposed leads to a better representation of concrete ductility under triaxial compression.

The use of a yielding criteria based on a second-degree function defines a yielding surface with curve meridians that accurately reproduces the variation of compression strength with the confinement pressure. The comparison with experimental results shows that this yielding surface is able to reproduce ultimate strength under compression for a fairly wide range of pressures.

As a result of the consideration of non-isotropic plastic hardening, with an initial yielding threshold surface more curved in the meridian planes than the ultimate strength surface, an increasing difference between initial yielding and ultimate strength is obtained for increasing confinement pressures. This result follows experimental evidence.

Acknowledgments

The financial support of CONICET, National University of Tucumán and Technological University is gratefully acknowledged. The authors also wish to thank the collaboration of Mrs. Amelia Campos in the English revision.

References

[1] Arya C, Clarke JL, Kay EA, O'Regan PD. TR 55: Design guidance for strengthening concrete structures using fibre composite materials: a review. Eng Struct 2002;24:889–900.
[2] Shahawya M, Mirmiran A, Beitelman M. Tests and modeling of carbon-wrapped concrete columns. Composites Part B 2000;31:471–80.
[3] Van Den Einde L, Zhao L, Seible F. Use of FRP composites in civil structural applications. Construct Buildg Mater 2003;17:389–403.
[4] Karabinis AI, Rousakis TC. Concrete confined by FRP material: a plasticity approach. Eng Struct 2002;24:923–32.
[5] Shao Y, Mirmiran A. Nonlinear cyclic response of laminated glass FRP tubes filled with concrete. Compos Struct 2004;65:91–101.

[6] Karabinis AI, Kiousis PD. Plasticity computations for the design of the ductility of circular concrete columns. Comput Struct 1996;60(5):825–35.
[7] Luccioni BM, Oller S, Danesi R. Coupled plastic damage model. Comput Methods Appl Mech Eng 1996;129:81–9.
[8] Balan T, Spacone E, Kwon M. A 3D hypoplastic model for cyclic analysis of concrete structures. Eng Struct 2001;23: 333–42.
[9] Untiveros C. Estudio experimental del comportamiento del hormigón confinado sometido a compresión. Ph.D. Thesis, Universitat Politecnica de Catalynya, Escola Técnica Superior D'Inginyers de Camins, Canals I Ports, Spain, 2002.
[10] Pantazopoulou SJ, Mills RH. Microstructural aspects of the mechanical response of plain concrete. ACI Mater J 1996;92(6):605–16.
[11] Pantazopoulou SJ. Role of expansion on mechanical behavior of concrete. ASCE J Struct Eng 1995;121(12): 1795–805.
[12] Sfer D, Carol I, Gettu R, Etse G. Study of the behavior of concrete under triaxial compression. J Eng Mech ASCE 2000;128(2):156–63.
[13] Mirmiran A, Shahawy M. Behavior of concrete columns confined by fiber composites. J Struct Eng ASCE 1997; 123(5):583–90.
[14] Samaan M, Mirmiram A, Shahawy M. Model of concrete confined by fiber composites. J Struct Eng ASCE 1998; 124(9):1025–31.
[16] Kwon M, Spacone E. Three-dimensional finite element analysis of reinforced concrete columns. Comput Struct 2002;80:199–212.
[17] Mirmiran A, Zagers K, Yuan W. Nonlinear finite element modeling of concrete confined by fiber composites. Finite Elements Anal Design 2000;35:79–96.
[18] Desai C, Zhang W. Computational aspects of disturbed state constitutive models. Comput Methods Appl Mech Eng 1998;151:361–76.
[19] Oller S. Un modelo de Daño Continuo para materiales Friccionales. Ph.D. Thesis, Universitat Politecnica de Catalynya, Escola Técnica Superior D'Inginyers de Camins, Canals I Ports, Spain, 2002.
[20] Lubliner J, Oliver J, Oller S, Oñate E. A plastic damage model for concrete. Int J Solids Struct 1989;25(3):299–326.
[21] Luccioni BM. Formulación de un modelo constitutivo para materiales ortótropos. Ph.D Thesis, Universidad Nacional de Tucumán, Argentina, 1993.
[22] Green A, Naghdi P. A general theory for an elastic–plastic continuum. Arch Rat Mech Anal 1964;18:19–281.
[23] Lubliner J. Plasticity theory. New York: MacMillan; 1990.
[24] Oliver J. A consistent characteristic length for smeared cracking models. Int J Numer Methods Eng 1989;28: 461–74.
[25] Oller S, Oliver J, Lubliner J, Oñate E. Un modelo constitutivo de daño plástico para materiales friccionales. parte I: variables fundamentales, funciones de fluencia y potencial. Revista Internacional de Métodos Numéricos para el Cálculo y Diseño en Ingeniería 1988;4:397–428.
[26] Chen W. Plasticity in reinforced concrete. McGraw-Hill; 1982.
[27] Kupfer H, Hilsdorf H, Rusch H. Behavior of concrete under biaxial stresses. ACI J 1969;66(8):656–66.
[28] Ahamd SH, Shah SP. Stress–strain curves of concrete confined by spiral reinforcement. ACI J 1982;79(6): 484–90.
[29] Tasuji E, Slate F, Nilson A. Stress–strain response and fracture of concrete in biaxial loading. ACI J 1978;75(7): 306–12.
[30] Toutanji H. Stress–strain characteristics of concrete columns externally confined with advanced fiber composite sheets. ACI Mater J 1999;96(3):397–404.
[31] O'Shea M, Bridge R. Design of circular thin-walled concrete filled steel tubes. ASCE J Struct Eng 2000; 126(11):1295–303.
[32] RILEM, Determination of the fracture energy of mortar and concrete by means of three-point bend test on notched beams. Mater Struct 1985;18(106):285–90.